Research Paper
J. Astron. Space Sci. 35(4), 235-242 (2018)
https://doi.org/10.5140/JASS.2018.35.4.235

JASS Journal of Astronomy and Space Sciences

First Comparison of Mesospheric Winds Measured with a Fabry-Perot Interferometer and Meteor Radar at the King Sejong Station (62.2°S, 58.8°W)

Wonseok Lee[1], Yong Ha Kim[1†], Changsup Lee[2], Qian Wu[3]

[1]Department of Astronomy, Space Science and Geology, Chungnam National University, Daejeon 34134, Korea
[2]Korea Polar Research Institute, Incheon 21990, Korea
[3]High Altitude Observatory, National Center for Atmospheric Research, Boulder, CO 80301, USA

A Fabry-Perot interferometer (FPI) for mesospheric observations was installed at King Sejong Station (62.2°S, 58.9°W) in Antarctica in 2017. For the initial validation of the FPI measurements, we compare neutral wind data recorded with the FPI with those from a Meteor Radar (MR) located nearby. The overall characteristics of the FPI and MR winds of both OH 892.0 nm (87 km) and OI 557.7 nm (97 km) airglow layers are similar. The FPI winds of both layers generally match the MR winds well on the observed days, with a few exceptions. The correlation analysis of the FPI and MR wind data shows that the correlation coefficients for the zonal winds at 87 and 97 km are 0.28 and 0.54, respectively, and those for the meridional winds are 0.36 and 0.54, respectively. Based on the assumption that the distribution of the airglow emissions has a Gaussian function with respect to the altitude, we calculated the weighted mean winds from the MR wind profile and compared them with the FPI winds. By adjusting the peak height and full width at half maximum of the Gaussian function, we determined the change of the correlation between the two winds. The best correlation for the OH and OI airglow layers was obtained at a peak height of 88–89 km and 97–98 km, respectively.

Keywords: mesosphere and lower thermosphere, Fabry-Perot interferometer, meteor radar, wind

1. INTRODUCTION

Temperature and wind observations are essential to understanding the dynamics and energy budget of the atmosphere. The mesosphere and lower thermosphere (MLT) are highly variable because of various wave activities in the lower atmosphere and several effects from space (Fritts & Alexander 2003). The determination of the exact temperature and wind in the MLT region is therefore of great importance. In the past, studies of the MLT region were significantly limited due to the inaccessibility of this region. With the development of various instruments (e.g., Meteor Radars; MRs, Fabry-Perot interferometers; FPIs, and medium-frequency radars), research about the MLT region has become more active compared with that a decade ago. A MR can measure neutral winds at altitudes ranging from 80 to 100 km throughout the year for 24 hr, regardless of the weather. Thus, the daily mean temperature near the mesopause can be estimated (Lee et al. 2016). An FPI is a very sensitive optical instrument that can measure airglow emissions at specific wavelengths (i.e., OH 892.0 nm, OI 557.7 nm, OI 630.0 nm) to simultaneously obtain both wind and temperature data at altitudes of airglow layers in the MLT region (e.g., Lee et al. 2017).

The King Sejong Station (KSS) in Antarctica (62.22°S, 58.78°W) has been operating an MR to study the neutral dynamics in the MLT region since 2007 (Jee et al. 2014). In addition, an FPI was installed at the KSS in 2017, making it possible to more actively conduct research on the MLT. Both instruments have the advantage of measuring neutral winds and temperatures in the MLT region, but the MR and FPI

Received 6 NOV 2018 **Revised** 22 NOV 2018 **Accepted** 23 NOV 2018
†**Corresponding Author**
Tel: +82-42-821-5467, E-mail: yhkim@cnu.ac.kr
ORCID: https://orcid.org/0000-0003-0200-9423

Table 1. Operating parameters of the KSS meteor radar

Parameter	Value
Frequency (MHz)	33.2
Frequency agility (kHz)	± 100
Transmit power (kW)	12
Transmit polarization	Circular
EPW (m/μs)	7,200/47.95
PRF (Hz)	440
Duty cycle (%)	8.4 %
Receiver-filter width (kHz)	18.1
Pulse code type	4-bit complementary
Pulse shape	Gaussian
Range (km)	80-306.8
Range sampling resolution (km)	1.8
Coherent integrations	4
Effective sampling time (sec)	0.009
Number of samples	12,650
Acquisition length (sec)	115

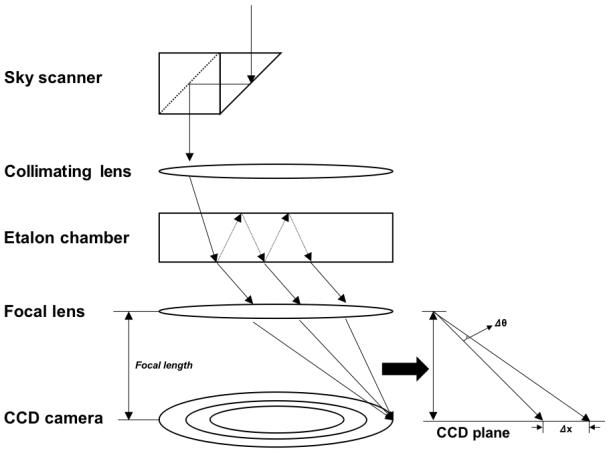

Fig. 1. Schematic structure of the FPI at the King Sejong Station (not in scale).

winds are obtained with fundamentally different methods. In case of the MR, the neutral wind data are derived from drifting information on meteor echoes observed in each altitude bin assuming that the meteor plasma trail moves together with the neutral atmosphere (Holdsworth et al. 2004). In case of the FPI, however, the underlying assumptions are that the height distribution of the airglow intensity remains constant and the winds are divergence-free within the field of view of the FPI during the observation.

In this study, we compare neutral wind data obtained with the FPI in the OH 892.0 nm and OI 557.7 nm airglow layers with winds simultaneously observed with the MR to confirm the reliability of the newly installed FPI. The instruments and measured wind data are described in Section 2. The results and a discussion are presented in Section 3. A conclusion is provided in Section 4.

2. INSTRUMENTS AND DATA

2.1 Meteor Radar

The MR at the KSS has been used to observe the MLT region since its installation in March 2007. Unlike other optical instru-ments, this instrument has the advantage of being able to continuously detect echoes from meteor trails for 24 hr, regardless of the daylight or weather conditions.

As a meteor enters the atmosphere, its kinetic energy is converted into thermal energy by the collision with atmospheric molecules and a cylindrical plasma trail forms in the path of the meteor. When the radio waves transmitted from the MR are perpendicular to the meteor trail, the radio signal scattered by electrons in the meteor trail is returned to the receiving antennae. Finally, the built-in analysis software is used to analyze the received signals and provides the altitude, distance, meteor speed, and radial velocity of the meteor echoes (Murad & Williams 2002). The background wind speed can be obtained from the radial velocity of the meteor echoes within 1 km and 1 hr bin using the least squares method (Holdsworth et al. 2004).

After upgrading the transmission power to 12 kW in 2012, the KSS MR has been able to detect 15,000–40,000 meteors per day with a notable seasonal dependence. The KSS MR operates at 33.2 MHz with a maximum duty cycle of 8.4 %. The analysis process is similar to that of the MR at Buckland Park (Holdsworth et al. 2004). Detailed operating parameters of the KSS MR are summarized in Table 1.

2.2 Fabry-Perot Interferometer (FPI)

The FPI was installed at the KSS in February 2017. The FPI includes two modules: an electronic module that controls an optical instrument and an optical module for the observation of airglow emissions. The structure of the FPI is shown in Fig. 1. The optical module is composed of a sky scanner, a filter wheel, an etalon chamber, focal lenses, and a CCD camera under the dome. All optical components, except for the sky scanner, are fixed to the optical frame, which is covered with a dark sheet as shield from stray light. As an initialization process of the observation, the sky scanner moves to the laser position. After the laser interference image of a calibration laser emission line (632.8 nm) is recorded in the CCD camera, regular airglow measurements are performed using three filters (OH 892.0 nm, OI 557.7 nm, OI 630.0 nm) for different airglow emissions. The OI 630.0 nm measurement is carried out with an exposure time of 5 min; the other measurements were performed with an exposure time of 3 min. Each measurement consists of an observation of the vertical (zenith) and cardinal points (north, south, east, and west). One observation cycle has a duration

Table 2. Cloud index information

Index	Cloud	Wind	Rain	Daylight
0	Unknown	Unknown	Unknown	Unknown
1	Clear (Sky T. < -35°C)	Calm (wind < 15 km/h)	Dry (impulse < 12)	Dark (unit < 121)
2	Cloudy (-25°C < Sky T. < -35°C)	Windy (15 km/h < wind < 30 km/h)	Wet (100 < impulse < 12)	Light (121 < unit < 220)
3	Very cloudy (-25°C < Sky T.)	Very windy (30 km/h < wind)	Rain (100 < impulse)	Very light (220 < unit)

*Sky T.: Sky temperature
*http://diffractionlimited.com/product/boltwood-cloud-sensor-ii/

of approximately 50 min. The observed data are analyzed with software developed by the High Altitude Observatory, National Center for Atmospheric Research, USA (Wu et al. 2012).

The principle of the FPI observation is as follows. First, the airglow enters the etalon chamber through the sky scanner. The monochromatic airglow light is captured in an interference image based on the repetition of transmission and reflection inside the etalon chamber. If the source of the airglow moves, that is, approaches or moves away from the observer, the incidence angle of the light forming the interference images becomes large or small, respectively. When the incidence angle of the light changes by $\Delta\theta$, the image on the CCD is displaced by $\Delta \boldsymbol{x} = f\Delta\theta$ (f: focal length). Thus, the drift velocity can be calculated using the Doppler shift (Wu et al. 2002, 2012).

Because the FPI observes the airglow light from the MLT region, it is critically affected by the weather conditions. Therefore, the wind and temperature data from the FPI for cloudy days are unreliable. A thorough data selection criterion must be established to control the data quality. The FPI is equipped with a cloud detector that uses infrared light to determine the amount of clouds. Details about the cloud index are presented in Table 2. Because the FPI also provides wind errors for the wind measurements, we used the data with wind errors below 20 m/s in this study (Section 3.1) to obtain large enough FPI wind data for the long-term comparison with the MR wind measurements. Beyond Section 3.1, we selected wind data with errors below 10 m/s and a cloud index 1 representing clear sky. As a result, only 16 % of the FPI wind data were used for the comparison.

3. RESULTS AND DISCUSSION

3.1 Comparison of Hourly Winds Measured by MR and FPI

Fig. 2 shows the hourly wind data at altitudes of 87 and 97 km measured by the FPI (with filters for OH 892.0 nm and OI 557.7 nm airglows) and MR as function of the day of year (DOY) and universal time (UT). The weather conditions defined by the cloud index significantly affect the wind error during FPI data analysis, resulting in a limited time coverage of the wind observations. Although the individual wind values from FPI and MR significantly differ from each other, their local time variations are in good agreement over the entire observation period in 2017. For example, both the FPI and MR simultaneously observed strong eastward zonal wind flow at 87 km (97 km) at ~02:00 UT (01:00 UT) and strong westward wind at ~07:00 UT. With respect to meridional wind, the two instruments measured consistent wind features; southward wind at ~01:00 UT (24:00 UT) at 87 km (97 km) and northward wind at ~05:00 UT (08:00 UT) at 87 km (97 km).

To compare the winds from the FPI with those from the MR on an hourly basis, we selected four independent days with continuous FPI wind measurements under good weather conditions. Fig. 3 shows the hourly wind vectors from the FPI at 87 and 97 km as a function of the UT and height. The wind vector fields from the MR for altitudes from 75 to 105 km are also presented. Although the FPI winds match the MR winds at 97 km, significant discrepancies are observed at 87 km.

For a quantitative comparison, we calculated the correlation coefficients between the FPI and MR winds. Fig. 4 displays the scatterplot of the hourly FPI winds and MR winds for the period from March to November 2017. The black and colored lines indicate the 1:1 line and regression line, respectively. The correlation coefficients are 0.28 for the zonal wind and 0.36 for the meridional wind at 87 km. The correlation coefficients are 0.54 for the zonal wind and 0.54 for the meridional wind at 97 km. They are significantly larger than those at 87 km, which will be discussed in Section 3.2. Another notable feature is that the FPI winds are consistently stronger than the MR winds in the two height layers, which may be due to the shorter time integration of the FPI than that of the MR. The FPI only needs 6 min to obtain a wind in a single direction, while the MR calculates one-hour average winds.

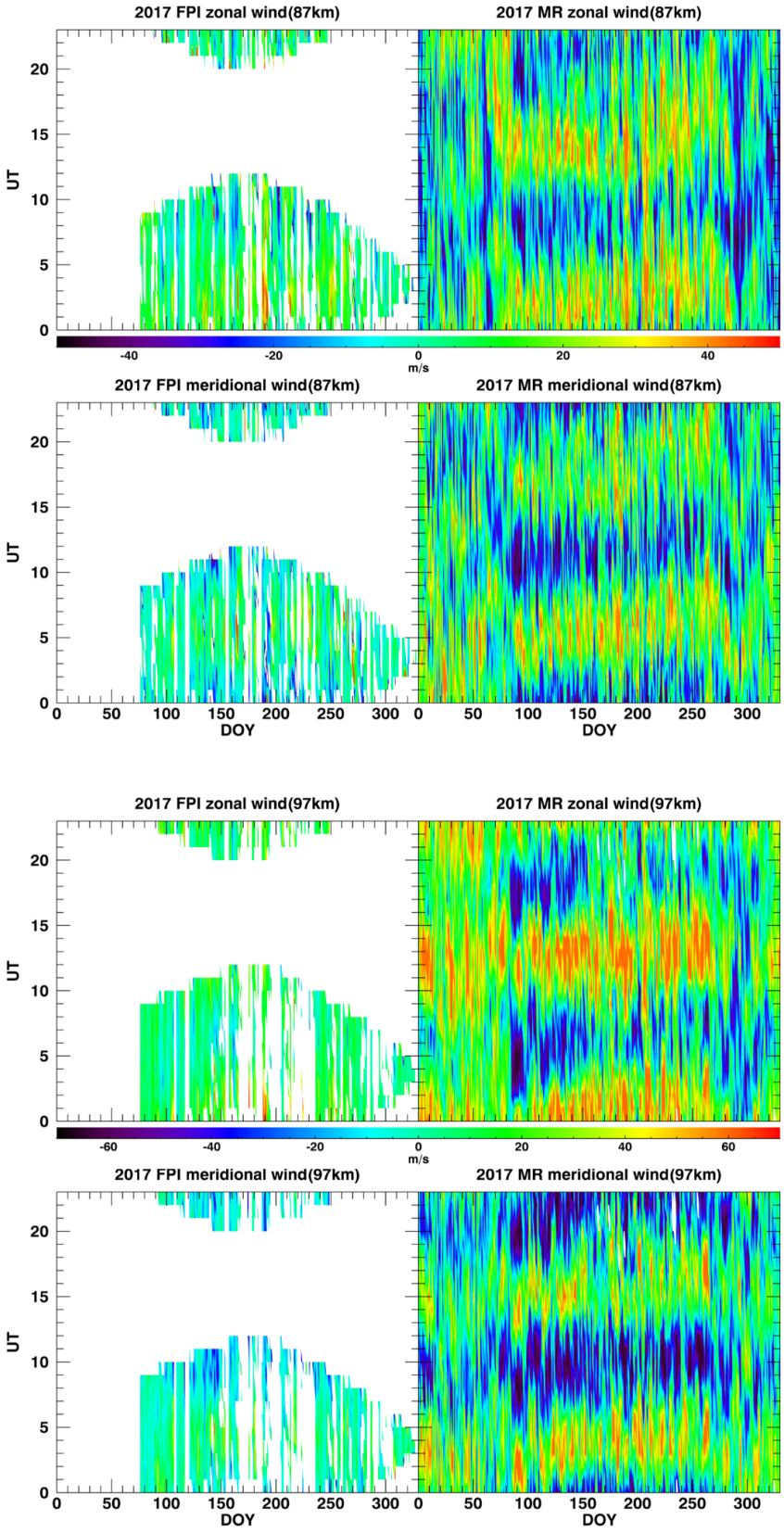

Fig. 2. Hourly neutral wind measured with the FPI (OH 892.0 nm and OI 557.7 nm) and MR (87 km, 97 km) as a function of the DOY and UT.

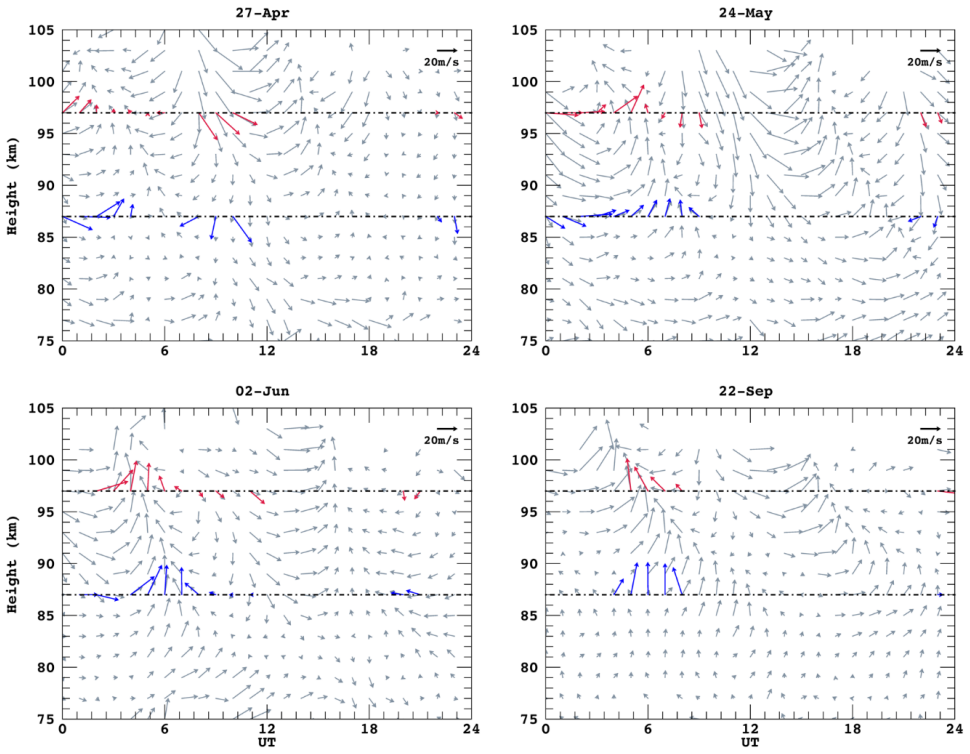

Fig. 3. Hourly FPI (red arrow: OI 557.7 nm, blue arrow: OH 630.0 nm) and MR (grey arrow) wind vectors as a function of the UT and height for four sampling days. The dash-dotted lines represent the nominal altitudes of the OI and OH airglow layers of 87 and 97 km, respectively.

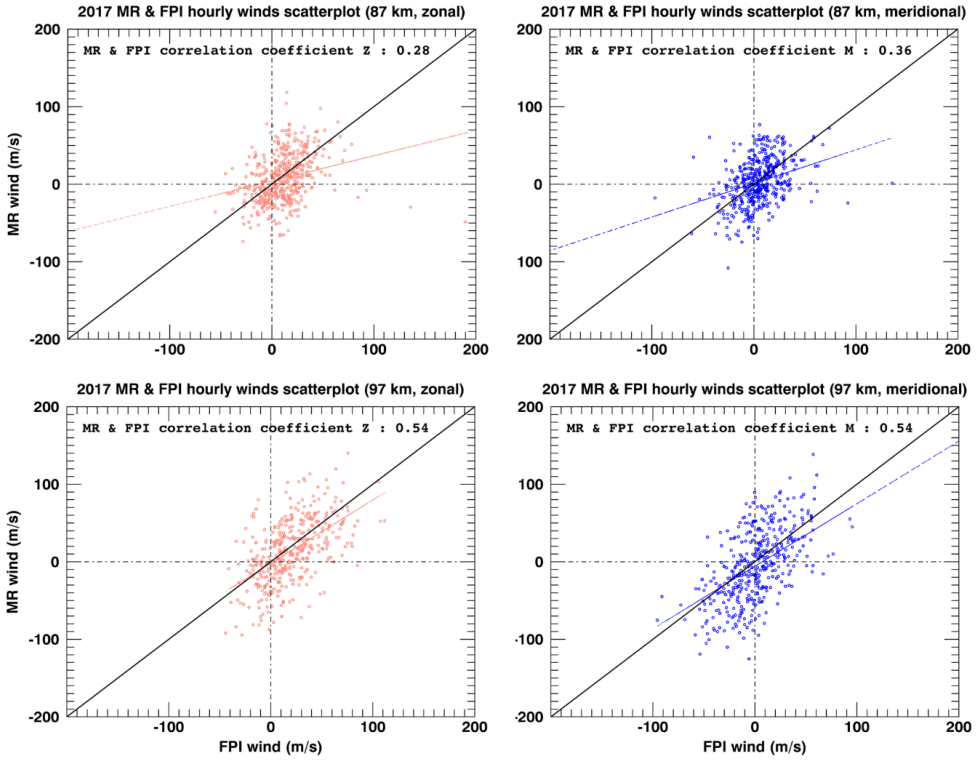

Fig. 4. Scatterplots between hourly FPI and MR winds observed from March to November 2017 at 87 km (upper panel) and 97 km (lower panel).

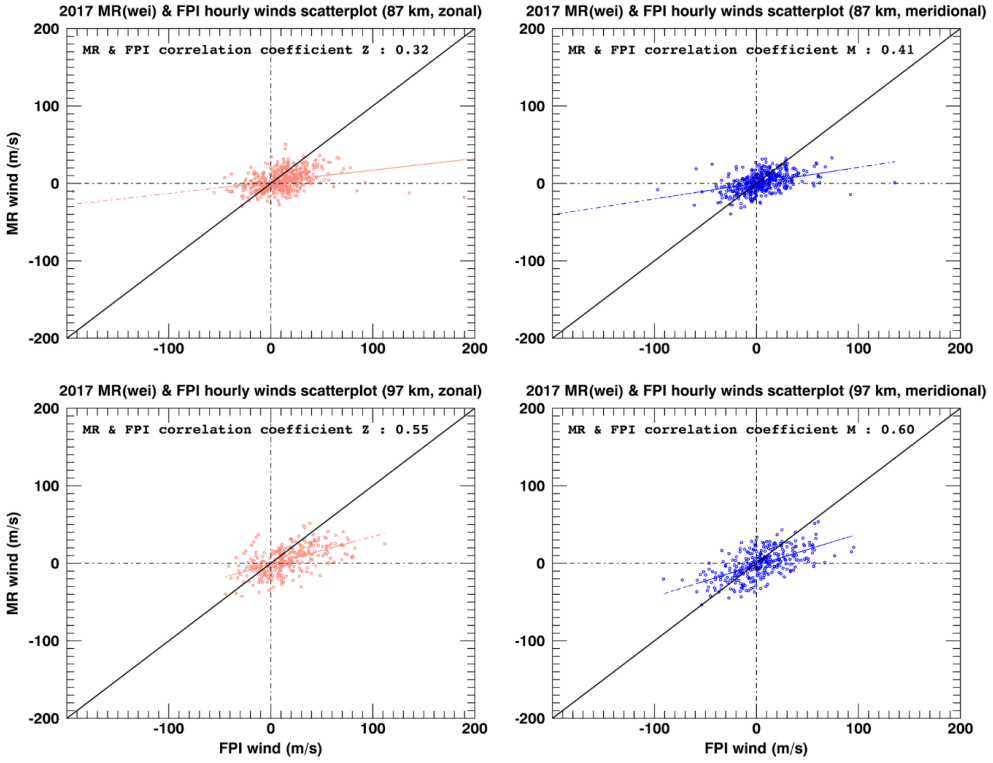

Fig. 5. Scatterplots between hourly FPI and weighted mean MR winds observed from March to November 2017 at 87 km (upper panel) and 97 km (lower panel).

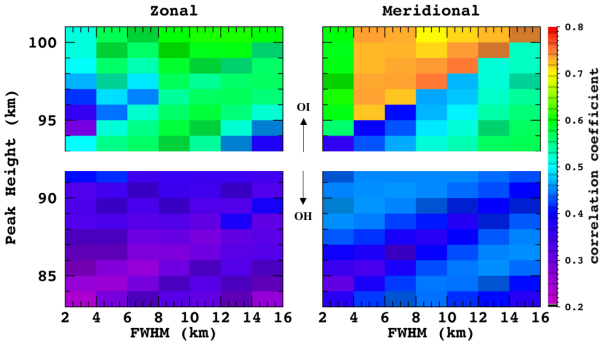

Fig. 6. Correlation coefficients between the FPI winds and weighted MR winds as functions of the FWHM and peak height. The FWHM's range from 2 to 16 km with a step size of 2 km and the peak heights of the OH (OI) layer vary from 83 km (93 km) to 91 km (101 km) with a step size of 1 km.

3.2 Comparison of FPI and Weighted Mean MR Winds

Because the FPI collects the emission from an airglow layer with a finite height, the FPI winds can be regarded as weighted mean values with the height distribution of the airglow intensities centered at 87 or 97 km, respectively. The full width at half maximum (FWHM) of the OH and OI airglow layers is ~10 km (Baker & Stair 1988; Yu et al. 2016). To consider the airglow height distribution in the comparison between the MR and FPI winds, we computed the weighted mean values of MR winds by assuming a Gaussian distribution with a FWHM of 10 km and peak height of 87 km and 97 km for the OH and OI layers, respectively.

Fig. 5 is similar to Fig. 4, but the FPI winds are compared with the weighted mean MR winds according to the airglow emission profile specified above. Overall, the correlation coefficients increase compared with those shown in Fig. 4. The correlation coefficients are 0.32 (0.55) for the zonal wind and 0.41 (0.60) for the meridional wind at 87 km (97 km). However, the absolute values of the weighted mean MR winds significantly decrease; therefore, the slopes of the fitting lines deviate from the 1:1 line.

To determine an optimal FWHM and central height for the airglow layer, we arbitrary varied the FWHM from 2 to 16 km with a step size of 2 km and the peak height of the OH (OI) layer from 83 km (93 km) to 91 km (101 km) with a step size of 1 km. Fig. 6 displays the correlation coefficients between the FPI and weighted mean MR winds for the aforementioned conditions. The correlation coefficient obtained by changing the FWHM at a fixed peak height of 87 km or 97 km shows no significant change. At a fixed FWHM of 10 km, the correlation coefficient considerably changes with the peak height; the highest correlation coefficient is obtained at a peak height of 88–89 km (97–98 km) for the OH (OI) airglow layer. This is consistent with peak height estimations for airglow layers

based on previous studies (Marsh et al. 2006; Yuan et al. 2013; Yu et al. 2017). We also note that the correlation coefficient of the OI layer is significantly higher than that of the OH layer. This result is opposite to that of Yu et al. (2016) who reported a much higher correlation coefficient for the OH layer compared with that for the OI layer. This discrepancy may be related to the unique location of the KSS. It is well known that the gravity wave activity is rather strong in the Antarctic Peninsula region (e.g., Wu & Jiang 2002; Lee et al. 2013). In fact, Kam et al. (2017) reported that the number of wave events at 87 km is significantly larger than that at 97 km over the KSS. In addition, Wu et al. (2013) showed that the gravity wave activity affects the airglow emissions below 88 km at Rothera (67°S, 68°W), a station neighboring the KSS. The spatial distribution of the airglow emissions may thus vary because of gravity waves (Manson et al. 1996).

4. SUMMARY AND CONCLUSION

The FPI was installed at the KSS, Antarctica, in 2017. To verify the reliability of the FPI data, we compared the FPI winds with MR winds that were simultaneously measured at the same location. The comparison of the first-year FPI wind dataset shows that the overall characteristics of the FPI winds are consistent with that of the MR winds at 97 km. The correlation coefficients between the two winds are 0.28 and 0.54 for the zonal component and 0.36 and 0.54 for the meridional component at 87 and 97 km, respectively. Because the FPI winds are weighted averages obtained along the height profile of the airglow emissions, we computed the weighted mean values of the MR winds by assuming a Gaussian function with a FWHM of 10 km and OH and OI airglow layer peak height of 87 km and 97 km, respectively. The correlation coefficients between the FPI and weighted MR winds improve, as expected, but the magnitudes of the weighted MR winds significantly decrease due to the averaging. We further investigated how the correlation changes depending on the assumed FWHM and peak height. The best correlation for the OH and OI airglow layers was obtained at a peak height of 86 km and 97–98 km, respectively. The best peak heights are consistent with that reported in other airglow studies. However, the overall correlation coefficients of the FPI winds with the MR winds are significantly lower than that of other studies based on FPI wind observations. This may be related to the strong wave activity over the Antarctic Peninsula. A further study will address the effect of the waves on the winds measured with the FPI.

ACKNOWLEDGMENTS

This work was supported by a fund from the Chungnam National University (2018).

REFERENCES

Baker DJ, Stair Jr AT, Rocket measurements of the altitude distributions of the hydroxyl airglow, Phys. Scr. 37, 611-622 (1988). https://doi.org/10.1088/0031-8949/37/4/021

Fritts DC, Alexander MJ, Gravity wave dynamics and effects in the middle atmosphere, Rev. Geophys. 41, 1003 (2003). https://doi.org/10.1029/2001RG000106

Holdsworth DA, Reid IM, Cervera MA, Buckland Park all-sky interferometric meteor radar, Radio Sci. 39, RS5009 (2004). https://doi.org/10.1029/2003RS003014

Jee G, Kim JH, Lee C, Kim YH, Ground-based observations for the upper atmosphere at King Sejong Station, Antarctica, J. Astron. Space Sci. 31, 169-176 (2014). https://doi.org/10.5140/JASS.2014.31.2.169

Kam H, Jee G, Kim Y, Ham Y, Song IS, Statistical analysis of mesospheric gravity waves over King Sejong Station, Antarctica (62.2° S, 58.8° W), J. Atoms. Sol.-Terr. Phys. 155, 86-94 (2017). https://doi.org/10.1016/j.jastp.2017.02.006

Lee C, Kim YH, Kim JH, Jee G, Won Yi, et al., Seasonal variation of wave activities near the mesopause region observed at King Sejong Station (62.22 S, 58.78 W), Antarctica, J. Atoms. Sol.-Terr. Phys. 105-106, 30-38 (2013). https://doi.org/10.1016/j.jastp.2013.07.006

Lee C, Kim JH, Jee G, Lee W, Song IS, et al., New method of estimating temperatures near the mesopause region using meteor radar observations, Geophys. Res. Lett. 43, 10580-10585 (2016). https://doi.org/10.1002/2016GL071082

Lee C, Jee G, Wu Q, Shim JS, Murphy D, et al., Polar thermospheric winds and temperature observed by Fabry-Perot interferometer at Jang Bogo Station, Antarctica, J. Geophys. Res. 122, 9685-9695 (2017). https://doi.org/10.1002/2017JA024408

Manson A, Yi F, Hall G, Meek C, Comparisons between instantaneous wind measurements made at Saskatoon (52N, 107W) using the colocated medium frequency radars and Fabry-Perot interferometer instruments: Climatologies (1988–1992) and case studies, J. Geophys. Res. 101, 29553-29563 (1996). https://doi.org/10.1029/96JD01915

Marsh DR, Smith AK, Mlynczak MG, Russel III JM, SABER observations of the OH Meinel airglow variability near the mesopause, J. Geophys. Res. 111, A10S05 (2006). https://doi.org/10.1029/2005JA011451

Murad E, Williams IP, Meteors in the Earth's Atmosphere

(Cambridge Univ. Press, Cambridge, 2002).
Wu DL, Jiang JH, MLS observations of atmospheric gravity waves over Antarctica, J. Geophys. Res. 107, ACL 14-1-ACL 14-6 (2002). https://doi.org/10.1029/2002JD002390
Wu Q, Killeen TL, McEwen D, Solomon SC, Guo W, et al., Observation of the mesospheric and lower thermospheric 10-hour wave in the northern polar region, J. Geophys. Res. 107, SIA 4-1-SIA 4-8 (2002). https://doi.org/10.1029/2001JA000192
Wu Q, Wang W, Roble RG, Häggström I, Strømme A, First daytime thermospheric wind observation from a balloon-borne Fabry-Perot interferometer over Kiruna (68N), Geophys. Res. Lett. 39, L14104 (2012). https://doi.org/10.1029/2012GL052533
Wu Q, Chen Z, Mitchell N, Fritts D, Limura H, Mesospheric wind disturbances due to gravity waves near the Antarctica Peninsula, J. Geophys. Res. 118, 7765-7772 (2013). https://doi.org/10.1002/jgrd.50577
Yu T, Xia C, Zuo X, Huang C, Mao T, et al., A comparison of mesospheric and low-thermospheric winds measured by Fabry-Perot interferometer and meteor radar over central China, J. Geophys. Res. 121, 10037-10051 (2016). https://doi.org/10.1002/2016JA022997
Yu T, Zuo X, Xia C, Li M, Huang C, et al., Peak height of OH airglow derived from simultaneous observations a Fabry-Perot interferometer and a meteor radar, J. Geophys. Res. 122, 4628-4637 (2017). https://doi.org/10.1002/2016JA023743
Yuan W, Liu X, Xu J, Zhou Q, Jiang G, et al., FPI observations of nighttime mesospheric and thermospheric winds in China and their comparisons with HWM07, Ann. Geophys. 31, 1365-1378 (2013). https://doi.org/10.5194/angeo-31-1365-2013